Acta Materialia 285 (2025) 120707

Contents lists available at ScienceDirect

Acta Materialia

journal homepage: www.elsevier.com/locate/actamat

Full length article

Hydrogen-assisted spinodal decomposition in a TiNbZrHfTa complex concentrated alloy

Chengguang Wu [a], Leonardo Shoji Aota [a], Jing Rao [a], Xukai Zhang [a], Loïc Perrière [b], Maria Jazmin Duarte [a], Dierk Raabe [a], Yan Ma [a,c,*]

[a] Max Planck Institute for Sustainable Materials, Max-Planck-Straße 1, Düsseldorf 40237, Germany
[b] CNRS, ICMPE, UMR 7182, Université Paris-Est Créteil, 2 rue Henri Dunant, Thiais 94320, France
[c] Department of Materials Science and Engineering, Delft University of Technology, Mekelweg 2, Delft 2628 CD, the Netherlands

ARTICLE INFO

Keywords:
Hydrogen
Refractory complex concentrated alloys
Spinodal decomposition
Thermodynamics
Phase stability

ABSTRACT

Understanding hydrogen-metal interactions is critical for developing refractory complex concentrated alloys (CCAs), applicable to the hydrogen economy. In this study, we revealed a hydrogen-assisted spinodal decomposition phenomenon at the nanoscale in an equiatomic TiNbZrHfTa CCA upon its exposure to H_2 at 500 °C. Such a decomposition pathway was characterized by a periodic compositional modulation with an up-hill diffusion behavior of the principal metallic elements, particularly Zr, over an extended treatment period (from 0.5 h to 2 h) in an H_2 atmosphere, probed by three-dimensional atom probe tomography. Consequently, the decomposed alloy consisted of a needle-shaped phase enriched in Zr and Ti and a phase enriched in Nb and Ta. Crystallographically, the spinodal features aligned preferentially along ⟨001⟩ directions of the matrix phase to minimize elastic strain energy. To better understand the role of hydrogen in spinodal decomposition, a statistical thermodynamic model was further developed by incorporating hydrogen to predict the phase stability of the TiNbZrHfTa-H system. This analysis suggested that hydrogen destabilizes the single solid-solution phase by expanding the spinodal region. Such nanoscale spinodal decomposition enhanced the hardness and anti-abrasive properties of the investigated alloy. Thus, this study not only provides fundamental insights into the effect of hydrogen on phase stability, but also demonstrates a novel alloy design strategy by introducing hydrogen as an interstitial alloying element to tailor the microstructure.

1. Introduction

Hydrogen has become attractive as a promising green energy source due to its potential to mitigate anthropogenic CO_2 emissions associated with the use of fossil fuels [1–3]. The deployment of hydrogen energy necessitates the development of advanced metallic alloys tolerating hydrogen-rich atmospheres, even at elevated temperatures [4–6]. Refractory complex concentrated alloys (CCAs), particularly those of the TiNbZrHfTa family have been recognized as potential candidates under such application conditions due to their extensive compositional design space and excellent mechanical properties (with a yield strength of ~300 MPa at 1000 °C) [7–10]. One of the key peculiarities in designing CCAs lies in the stabilization of a single-phase solid solution depending on the maximization of configuration entropy [11–13]. However, phase decomposition via secondary phase precipitation and ordered phase formation has been frequently observed in some refractory CCAs after heat treatment [14–16].

Hydrogen is bound in various chemicals, such as H_2, NH_3, and hydrocarbons, *etc*. It is worth noting that the size of a neutral H^0 atom, as measured by the Bohr radius, is only 0.529 Å [17]. This enables hydrogen to readily enter metal lattices, especially for loosely packed body-centered cubic (BCC) metals like refractory CCAs with a packing density of 68 % [18–20]. This feature facilitates hydrogen diffusion and interaction with host metallic atoms in bulk materials. Additionally, the medium electronegativity of hydrogen (2.2) allows it to form various kinds of chemical bonds (ionic bond and covalent bond) with metallic elements [17,21]. Hydrogen has long been treated as a detrimental element for structural materials, which can cause catastrophic failure of metallic components, known as hydrogen embrittlement [22–24]. Moreover, hydrogen forms metal hydrides with several alkali (*e.g.*, Li, Na, K), alkaline earth (*e.g.*, Mg), and refractory (*e.g.*, Ti, Zr, Hf) metals via the reversible phase transformation, which is the basis of hydrogen

* Corresponding author.
E-mail address: y.ma@mpie.de (Y. Ma).

https://doi.org/10.1016/j.actamat.2024.120707
Received 10 September 2024; Received in revised form 16 November 2024; Accepted 31 December 2024
Available online 2 January 2025

storage materials [7,25,26]. Therefore, a better understanding of the interaction between hydrogen and constituent metallic elements in refractory CCAs is essential for optimizing their composition and microstructure suited for applications in hydrogen-rich environments as structural or hydrogen-storage materials.

In this study, nanoscale spinodal decomposition is observed in an equiatomic TiNbZrHfTa CCA upon exposure to H_2 at 500 °C for 0.5 h, resulting in two phases enriched in Ti/Zr and Nb/Ta, respectively. A statistical thermodynamic model incorporating hydrogen has been developed to elucidate the mechanisms of such hydrogen-assisted spinodal decomposition. The hydrogen acquired from the environment expands the spinodal region of TiNbZrHfTa CCAs, thus promoting spinodal decomposition. Our findings highlight the significant role of hydrogen in altering the thermodynamic boundaries by expanding the spinodal decomposition region in the TiNbZrHfTa alloy. The spinodal features improve the hardness and wear resistance. This study provides a novel strategy for designing spinodal-strengthed refractory CCAs by deploying acquired hydrogen from the environment to modify the thermodynamic conditions of the alloy system and modulate local chemical and structural patterns at the nanoscale.

2. Methods

2.1. Material fabrications

The five-component TiNbZrHfTa complex concentrated alloy (CCA) with an equiatomic ratio was fabricated using the corresponding pure metals with a purity of 99.95 wt.% by arc melting under an Ar atmosphere. To ensure the homogeneity of the constituent elements, the ingots were remelted at least five times during the arc-melting process. A piece of Ti getter was placed in the arc melter to avoid potential oxygen contamination. The as-cast material was cold-rolled down to ~1.2 mm with a thickness reduction of 80 %. Subsequently, the material was annealed at 1100 °C for 5 h in a He-filled quartz tube, followed by forced cooling outside the furnace (air quenching), which was referred to as the as-received state in this study. The as-received specimens were exposed to pure H_2 gas with a purity of 99.999 % in a thermal dilatometer (DIL 805A/D, TA Instruments, USA). Before the exposure to H_2 gas, the DIL chamber was evacuated by a vacuum pump to a pressure below 10^{-6} bar. Then H_2 gas was introduced into the DIL chamber up to 0.8 bar. The specimens were heated with the induction coil to 500 °C with a heating rate of 20 °C/min. The isothermal treatments were conducted for 0.5 h, 1 h, and 2 h, followed by furnace cooling. The corresponding samples were referred to as HT-H_2, HT-H_2-1h, and HT-H_2-2h, respectively. In addition, a reference specimen was exposed to pure Ar (99.999 % purity) at 500 °C for 0.5 h, referred to as HT-Ar sample.

2.2. Materials characterizations

The dissolved hydrogen and oxygen contents of the as-received, HT-Ar and HT-H_2 specimens were determined by a melt extraction method using the GALILEO G8 ONH (Bruker, Germany) equipment. The measurements were performed immediately after heat treatment with a transferring time shorter than 12 h. The specimen surfaces were ground with 1000-grit SiC paper to eliminate the surficial oxide layer during sample transfer. Measurements were conducted at a power of 35 %, using tin baskets as the carrier. A thermal conductivity detector was employed to detect the hydrogen and oxygen contents, and helium was used as the carrying gas.

To identify crystal structures and quantify phase compositions, synchrotron high-energy X-ray diffraction (HEXRD) experiments were performed at the Powder Diffraction and Total Scattering Beamline, P02.1, of PETRA III at Deutsches Elektronen-Synchrotron (DESY, Hamburg). HEXRD profiles were acquired with a fixed beam energy of ~60 keV ($\lambda = 0.207354$ Å) and processed with the aid of the GASA-II software [27].

The microstructures of the as-received and heat-treated samples were characterized by backscattered electron (BSE) imaging, energy dispersive X-ray spectroscopy (EDS), and electron backscatter diffraction (EBSD) techniques using a Zeiss Merlin scanning electron microscope (SEM). Specimens for SEM characterization were mechanically ground (from 400 to 4000 grits of SiC papers) and polished with 30 vol. % H_2O_2-contained colloidal silica suspension solution until a mirror-finish surface was obtained. EBSD data was acquired at an acceleration voltage of 15 kV with a step size of 0.1 μm. The datasets were analyzed using the software OIM Analysis™ V8.0.

The nanoscale structures were further characterized using an image-corrected transmission electron microscopy (TEM, Titan Themis G2 300). The TEM specimens were prepared by the focused ion beam (FIB) lift-out method using the FEI Helios NanoLab 600i dual-beam FIB/SEM instrument. The TEM images were acquired at an acceleration voltage of 300 kV along the [001] zone axis. The local strain map was obtained from geometric phase analysis (GPA) using the open-source program Strain++ [28]. Atom probe tomography (APT, CAMECA LEAP 5000 XR) was employed to investigate the elemental distribution at a near-atomic scale. The sharp-tip specimens were prepared by lift-out and annular milling procedures using the FIB. All the APT measurements were conducted under laser mode with a base temperature, laser energy, pulse rate, and detection rate of 70 K, 60 pJ, 100 kHz, and 0.5 %, respectively. The reconstruction of the three-dimensional atom maps and data analysis were conducted using the commercial software AP Suite 6.1.

2.3. Microhardness and scratch tests

The Vickers hardness measurements were performed using Zwick-Roell ZHV10 hardness testing machine with a load of 0.2 kg. A minimum of six indents were collected for each specimen, and the data was shown as the mean Vicker hardness values (HV0.2) plus the standard deviation. The wear behavior was evaluated in the Keysight G200 nanoindenter using a 5-μm-radius spherical diamond tip. The scratch tests were conducted with a constant load of 20 mN in ambient air and a wear velocity of 1 μm/s. The depth of the scratch was characterized using the same diamond tip with a force of 0.1 mN before and after scratch tests, while the surface topography was captured using white-light confocal microscopy.

3. Results

3.1. Hydrogen-assisted spinodal decomposition

The as-received TiNbZrHfTa sample reveals a single BCC phase with a lattice parameter of 3.406 Å, as suggested by the HEXRD profile (Fig. 1a). Upon the heat treatment in H_2 atmosphere at 500 °C for 0.5 h, a large amount of hydrogen is absorbed by the TiNbZrHfTa CCA, which was quantified to be 8.60±0.41 at.% by TDS analysis. This content surpasses those in the as-received and HT-Ar samples by a factor of 19 and 8, respectively (**Table S1** and **Fig. S1**). The HEXRD measurements suggest that the HT-H_2 sample maintains a BCC crystal structure and no formation of hydride is observed in Fig. 1a. These facts are supposed to be due to the high solubility of hydrogen in these principal elements (for instance, 54.55 at.% for β-Zr) [29]. Nevertheless, the diffraction peaks of the HT-H_2 sample shift to lower Bragg angles and become asymmetric (Fig. 1b). Such peak shift indicates an increase in the lattice parameter, and peak asymmetry suggests that two BCC phases possibly co-exist with different lattice parameters. For instance, the (211) peak can be deconvoluted into two peaks (Fig. 1d). From the Rietveld refinement on the full HEXRD profile, the BCC Phase 1 with a lattice parameter of 3.414 Å (a_1) accounts for 56.0 wt.%, and the amount of BCC Phase 2 with a lattice parameter of 3.398 Å (a_2) is 44.0 wt.%.

Microstructures were further evaluated by coupling BSE and EBSD analyses (Fig. 2 and **Fig. S2**). The as-received sample shows an equiaxed grain morphology (Fig. 2a) with a grain size of 78.79±27.40 μm

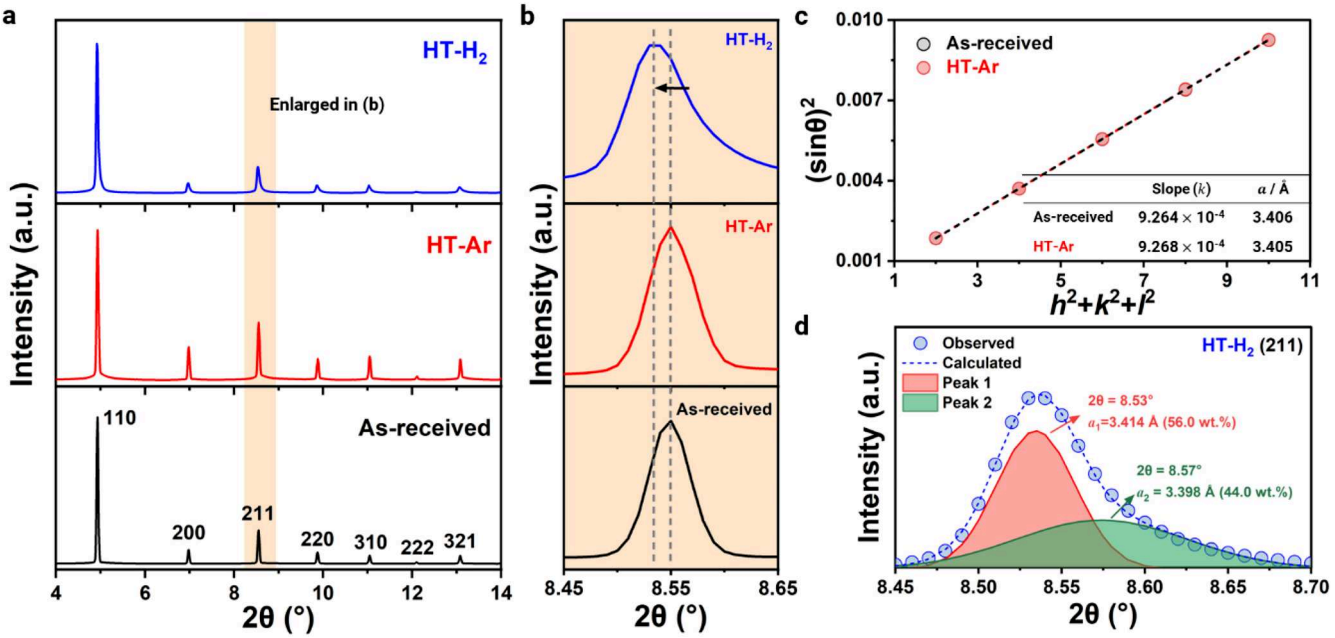

Fig. 1. (a) Overall high-energy X-ray diffraction (HEXRD) profiles and (b) enlarged views of BCC_{211} peaks of the as-received, HT-Ar, and HT-H_2 specimens. (c) The plot of $(sin\theta)^2$ as a function of $(h^2+k^2+l^2)$ of individual HEXRD peaks to determine the lattice parameters of the as-received and HT-Ar samples. (d) Enlarged image showing the deconvolution of BCC_{211} peaks of the HT-H_2 specimen.

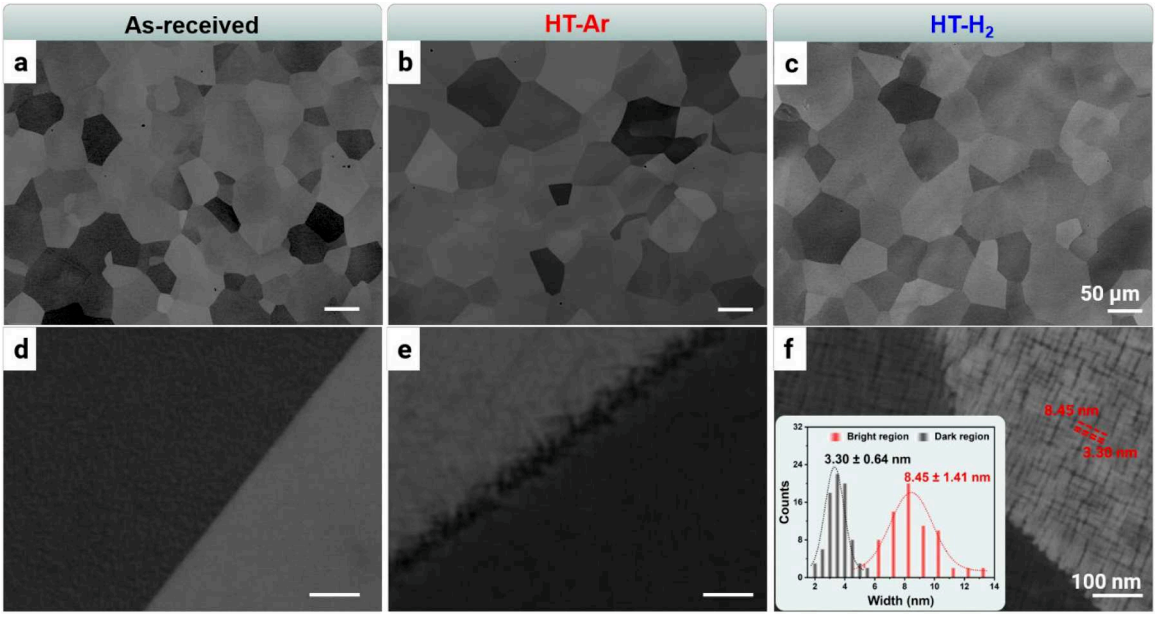

Fig. 2. Backscattered electron (BSE) and representative enlarged images of (a, d) as-received, (b, e) HT-Ar, and (c, f) HT-H_2 samples, respectively. Insert in (f) shows the width distribution of regions with dark (black) and bright (red) contrast. (For interpretation of the references to colour in this figure legend, the reader is referred to the web version of this article.)

(**Fig. S2**g). The inverse pole figure reveals that grains are randomly oriented and high-angle grain boundaries (>15°) constitute the major type of interfaces (>80 %, **Fig. S2**a), suggesting the complete recrystallization of the as-received sample. After heat treatment in H_2 and Ar gases, the HT-H_2 and HT-Ar samples maintain identical microstructural features compared with the as-received sample, in terms of grain morphology, size, and crystallographic orientation (Figs. 2a-c and **Fig. S2**). EDS elemental mapping across multiple grains confirms a spatially uniform distribution of all five constituent elements at the microscopic scale in all three samples (**Fig. S3**), and the bulk composition is determined to be $Ti_{22.95}Nb_{18.93}Zr_{20.89}Hf_{18.22}Ta_{19.01}$ (in at.%). These findings imply that heat treatment under both H_2 and Ar atmospheres has a negligible impact on structure and composition at the microscopic scale.

At a higher magnification down to the nanometer scale, two distinct regions are identified in a modulated pattern in the HT-H_2 sample, as observed in terms of dark and bright contrast, respectively, in Fig. 2f. The dark regions with a width of 3.30±0.64 nm are homogeneously distributed and intersect at an angle of approximately 90°. The bright features with a width of 8.45±1.41 nm interweave with the dark regions. Such an interwoven pattern was also observed using TEM, as shown in the bright-field image (Fig. 3a). The width of the bright and

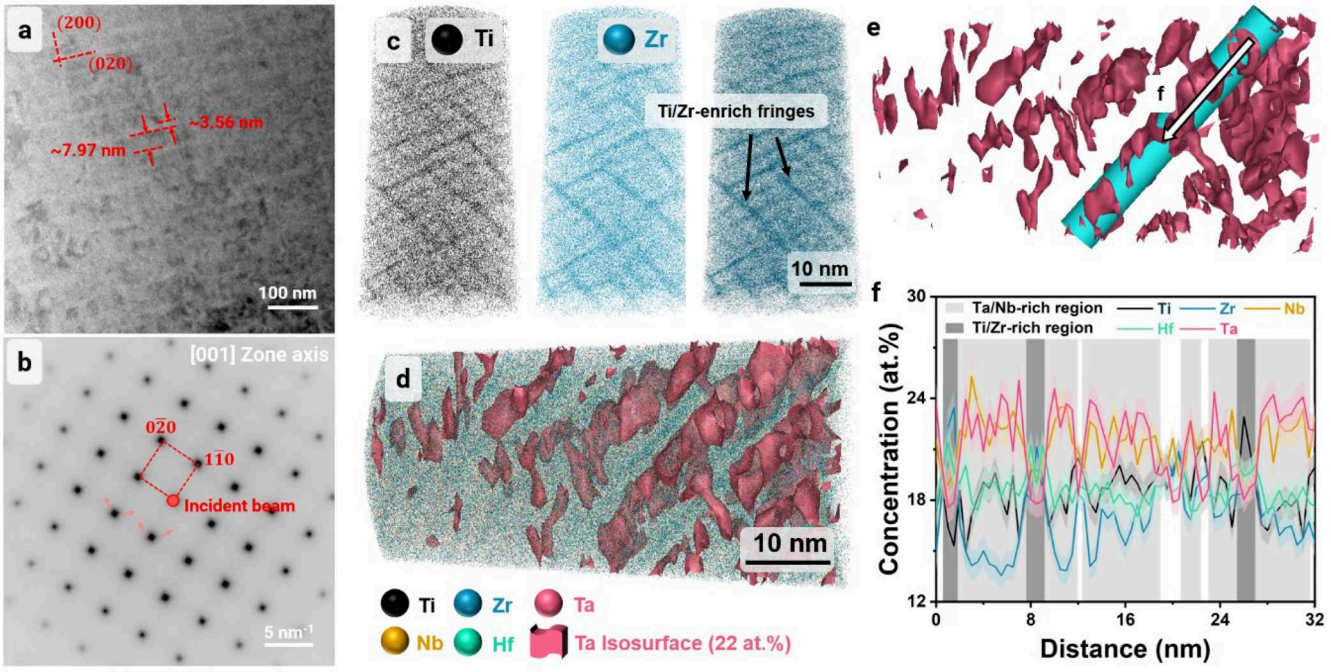

Fig. 3. (a) Typical bright-field transmission electron microscopy (TEM) image, and the corresponding (b) selected area electron diffraction pattern exhibiting a single BCC phase. The electron beam is along the [001] zone axis. Three-dimensional reconstruction map of (c) Ti distribution, Zr distribution, and superimposed Ti and Zr distribution probed by atom probe tomography (APT). (d, e) APT maps showing the Ta-rich nanofeatures in the matrix. The Ta-rich nanofeatures are highlighted using iso-concentration surfaces containing 22 at.% Ta. (f) Concentration profiles computed along the cyan cylinder marked in (e) with a binning size of 0.5 nm. The error bar represents the standard deviation of the counting statistics in each bin.

dark regions are quantified to be 3.56 nm and 7.97 nm, respectively, which concur well with the SEM observations (Fig. 2f). These interwoven structures are crystallographically aligned along the ⟨100⟩ directions, as determined by TEM analysis. Such an orientation dependence minimizes elastic strain energy in the TiNbZrHfTa alloy (see Supplementary Note 1) [30,31]. The selected area electron diffraction in Fig. 3b also reveals a BCC crystal structure of the HT-H_2 sample and no secondary crystal structure is observed, being consistent with the HEXRD results. Thus, the contrast in Figs. 2f and 3a is primarily attributed to the inhomogeneous elemental distribution, as particularly

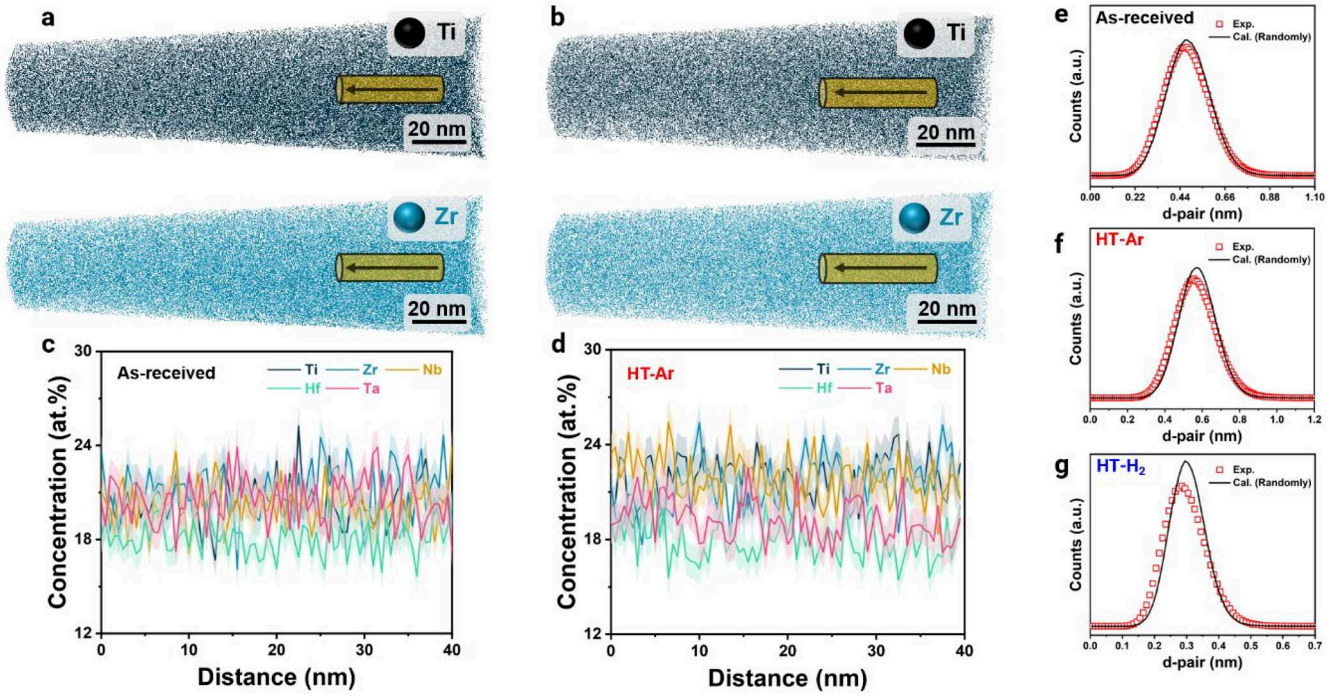

Fig. 4. Three-dimensional APT maps of the distribution of Ti and Zr in (a) as-received and (b) HT-Ar specimens. Concentration profiles of principal elements along the yellow cylinders in (c) as-received and (d) HT-Ar specimens, respectively. The fifth nearest neighboring distribution of Ti atoms of (e) as-received, (f) HT-Ar, and (g) HT-H_2 specimens, respectively. (For interpretation of the references to colour in this figure legend, the reader is referred to the web version of this article.)

the backscattered electron signal is sensitive to chemistry.

To further assess the elemental distribution in the HT-H_2 sample, we employed APT, which allows for local chemical analysis down to near-atomic resolution. The overall composition of the HT-H_2 specimens is determined to be $Ti_{19.66\pm0.91}Nb_{21.02\pm0.91}Zr_{19.05\pm0.90}Hf_{19.05\pm0.06}Ta_{19.45\pm0.33}$ (in at.%) by averaging the composition over three APT tips, agreeing with the nominal bulk composition. The three-dimensional elemental distribution maps, *e.g.*, Ti and Zr maps (Fig. 3c), reveal a nano-structured interwoven pattern, similar to that observed in the BSE and TEM images. Two regions are distinguished by the periodic chemical modulation. A needle-shaped region with an average width of ~1.0 nm is enriched in Ti (21.34±0.73 at.%) and Zr (22.88±0.82 at.%), yet depleted in Ta (17.72±1.56 at.%) and Nb (19.20±0.33 at.%) as shown in Figs. 3c and f. The other region, marked by the iso-concentration surface of 22 at.% Ta (Fig. 3d), is depleted in Ti (16.86±0.78 at.%) and Zr (14.41±0.59 at.%), while it is enriched in Ta (23.85±1.46 at.%) and Nb (23.10±1.15 at.%). The average width of this Ta/Nb-rich region is about 4.0 nm. Such a nano-scale elemental separation is primarily attributed to the relatively low quantity of mixing enthalpy between Ti and Zr as well as Nb and Ta [32]. In comparison, the periodically modulated chemical pattern is not observed in the APT tips of the as-received and HT-Ar specimens (Fig. 4), where all five principal elements are homogeneously distributed in the whole tips. Moreover, the clustering behavior in the HT-H_2 sample is confirmed by the nearest neighboring distribution, describing the probability of another Ti atom existing within some distance of a Ti atom [33–35]. As shown in Figs. 4e-g, the experimental line of the HT-H_2 sample does not match well with the calculated line that indicates the random distribution of Ti atoms, suggesting the clustering of Ti atoms. Similar trends can be obtained from the μ-values extracted from the APT datasets (**Fig. S4**). μ-value reflects the local clustering of the principle element, where it is indicative of element clustering when μ closes to 1, while it means random distribution of elements when μ closes to 0 [36,37]. The μ-values for each principle element of the HT-H_2 specimen are larger than those of the other two specimens, suggesting the clustering and redistribution of elements in the HT-H_2 sample.

Based on the above results, the original BCC matrix decomposes into two BCC phases with distinctive lattice parameters (a_1 and a_2) and constituent elements (enriched in Ti/Zr and Nb/Ta) after heat treatment under H_2. The process of this decomposition can proceed either via a nucleation and subsequent growth pathway or by a spontaneous spinodal decomposition without nucleation [38]. The nuclei for the nucleation pathway are formed with an equilibrium concentration (or deviate from the tie-line concentration for the case of a multicomponent system) in the initial state, maintaining this concentration (or evolving towards the equilibrium concentration) throughout the coarsening process [38–41]. In such cases, a sharp change in local concentration can be anticipated. In contrast, the spinodal decomposition amplifies with time, and the local concentration gradually deviates from the initial concentration until the equilibrium concentration is attained [42]. Thus, the amplifications of local composition over time (0.5, 1, 2 h) for heat treatment in H_2 are investigated to elucidate the decomposition process in the present TiNbZrHfTa CCA. The characteristic uphill diffusion behavior of elements over time rationalizes a spinodal decomposition process, rendering the periodically modulated chemical pattern of the TiNbZrHfTa alloy treated in the H_2 atmosphere (Fig. 5). While the alloy

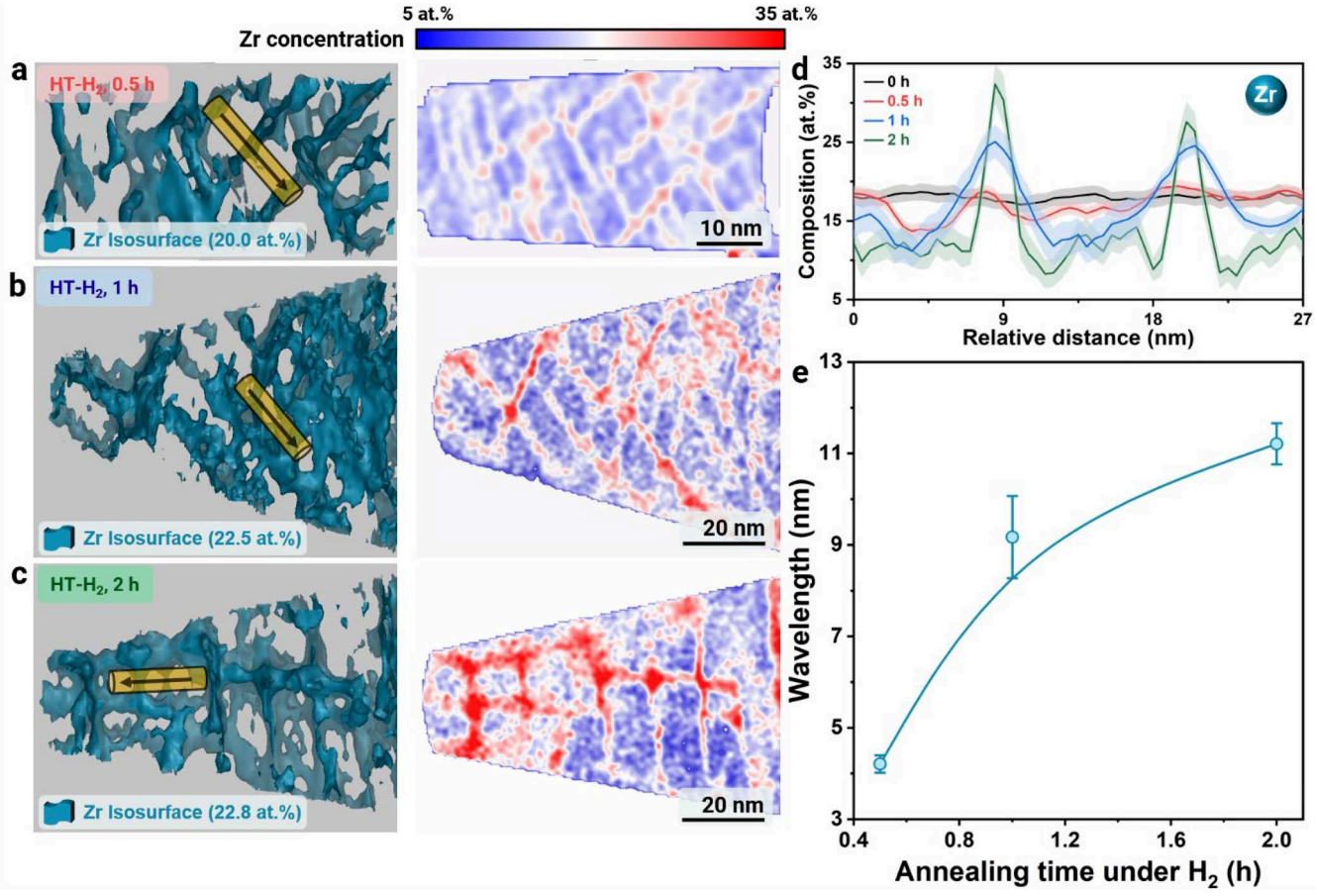

Fig. 5. APT reconstruction of Zr iso-concentration surfaces of the specimens treated in H_2 for (a) 0.5 h, (b) 1 h, and (c) 2 h and the corresponding two-dimensional contour plots. (d) Concentration profiles of Zr along the yellow cylinders marked in (a-c), the error bar represents the standard deviation of the counting statistics in each bin of the cylinder. (e) Evolution of spinodal wavelength with annealing time under H_2. (For interpretation of the references to colour in this figure legend, the reader is referred to the web version of this article.)

maintains a BCC crystal structure (**Fig. S5**), an interwoven chemical pattern gradually develops with prolonged treatment durations. As exemplified by the Zr concentration profile, Zr concentration increases over time (0.5, 1, 2 h) in the needle-shaped region from 21.70 at.% at 0.5 h, to 27.07 at.% at 1 h, and reaching 34.39 at.% at 2 h (Fig. 5d). Such an uphill diffusion behavior and the isostructure of the Ti/Zr-rich and Ta/Nb-rich regions (*i.e.*, both in BCC crystal structure with coherent interface) characterize a spinodal decomposition pathway [38,39,43]. An increase in the wavelength of the spinodal decomposition over annealing time under H_2 is observed, evolving from the initial 4.21 ±0.19 nm (0.5 h) to 9.17±0.90 nm and 11.21±0.45 nm for the HT-H_2-1h and HT-H_2-2h specimens, respectively (Fig. 5e and **Fig. S6**) [44,45]. Such a hydrogen-assisted phase decomposition phenomenon has not been reported in the literature. Its underlying mechanism will be discussed in the **Discussion Section**.

3.2. Enhancement in hardness and wear resistance via hydrogen-assisted spinodal decomposition

The hydrogen-assisted spinodal composition results in confined nanostructuring, associated with the generation of a periodic strain field (Figs. 6a and b). The crystal lattices of two isostructural phases possess slightly different lattice parameters (Δ = 0.007 nm), due to the different atomic radii of Zr (0.155 nm) from those of Nb (0.145 nm) and Ta (0.145 nm) [46]. Thus, the coherent interface of the periodic isostructural phases is characterized by a subtle strain misfit of ~0.2 % (Fig. 6b). Such a feature is attractive in enhancing mechanical properties [47,48].

The micro Vickers hardness of the TiNbZrHfTa alloy is shown in Fig. 6c. The hardness values are similar for the as-received (312.10 ±5.03 HV0.2) and the HT-Ar (301.00±28.43 HV0.2) specimens. In contrast, the heat treatment in the H_2 atmosphere (HT-H_2) increases the hardness by ~91 HV0.2 to 401.83±27.92 HV0.2. Hydrogen is considered as a strengthening element in Ti alloys mainly due to its solid solution strengthening effect, and the occurrence of hydrogen-induced secondary phase formation [49–51]. For solid solution strengthening, the increment in yield strength (σ) is proportional to the hydrogen concentration ($\Delta\sigma \propto \sqrt{c_H}$, c_H is the H concentration). In addition, hydrogen will increase the lattice strain (ϵ), thus leading to larger lattice distortions which enhance the friction stress in the material [52]. In our case, the hydrogen concentration inside the alloy drops down to 108 ppm before the hardness measurement (one week after hydrogen charging) due to the high hydrogen diffusivity (~10^{-10} m^2/s for β-Ti) [53]. The HEXRD results shown in Fig. 1 exhibit no significant change in lattice parameters between the HT-H_2 and the as-received specimen states. These results suggest that the solid solution strengthening effect from hydrogen is negligible in this specific case. Additionally, from our experimental results (Figs. 1 and 2a), besides spinodal phases, no other secondary phases can be detected. Therefore, the enhanced hardness is

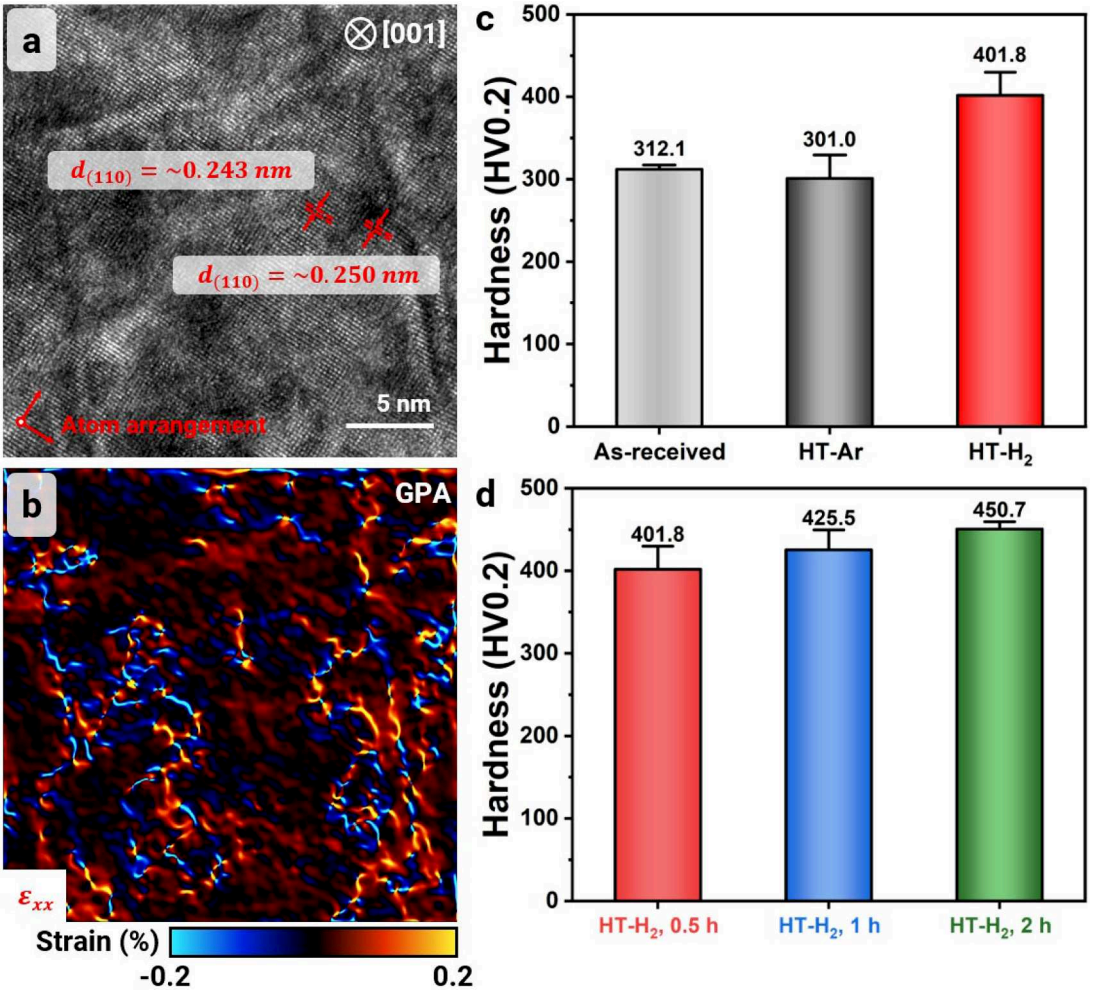

Fig. 6. (a) Image-corrected high-resolution TEM (HR-TEM) image of the HT-H_2 specimen along [001] zone axis. (b) Map of strain distribution (ε_{xx}) of the HT-H_2 specimen determined by geometric phase analysis (GPA) of HR-TEM image from the same area in (a). (c) Hardness (HV0.2) of as-received, HT-Ar, and HT-H_2 specimens after the heat treatment (hardness measurements were conducted one week after the heat treatment). (d) Hardness (HV0.2) evolution of specimens treated in H_2 at 500 °C for 0.5 h (HT-H_2), 1 h (HT-H_2-1h), and 2 h (HT-H_2-2h).

supposed to be predominantly ascributed to the hydrogen-assisted spinodal decomposition effect. The strengthening effect of the spinodal features can be derived from both lattice misfit strengthening and modulus strengthening based on Kato's model [54]:

$$\Delta\sigma = \frac{A\kappa Y}{2} + \frac{0.65\Delta G b}{\lambda} \quad (1)$$

where A stands for the amplitude of composition modulation ($A = 0.08$, Fig. 3f), while κ is the variation in lattice constant ($\kappa = 0.063$, Fig. 1d) with respect to the composition fluctuation. $Y = (C_{11}+2C_{12})(C_{11}-C_{12})/C_{11}$ is related to the elastic constant C_{ij} [47], ($Y = 55.7$ GPa based on literature data [55]), and ΔG stands for the amplitude of the shear modulus fluctuation ($\Delta G = 3.1$ GPa). b denotes the Burgers vector ($b = 2.942 \times 10^{-10}$ m determined from Fig. 1a) and λ is referred to the wavelength of modulation ($\lambda = 4.2 \times 10^{-9}$ m, Fig. 5e). Thus, the spinodal decomposition predominantly yields a misfit strengthening effect of ~140 MPa and a modulus strengthening effect of ~141 MPa, resulting in a total increase in strength ($\Delta\sigma$) of ~281 MPa. Using a conversion factor between hardness and yield strength of $\Delta HV0.2 \approx 3{\cdot}\Delta\sigma$ [56,57], an increment in hardness is thus predicted to be 84.3 HV0.2 (the unit of microhardness is converted by 1 HV = 10 MPa). The measured value of the hardness increased by 91 HV0.2 agrees well with this predicted value. Moreover, the hardness is further enhanced with prolonged heat treatment in H_2 associated with the intensified composition fluctuation (Fig. 6d).

The wear behavior of the as-received and HT-H_2-2h samples was also studied by scratch tests. As revealed by the three-dimensional morphology of the wear surfaces using confocal microscopy (Figs. 7a-c), the HT-H_2-2h sample reveals a narrow (2.38 μm in width) and shallow (210 nm in depth) wear track, which is profoundly different from the wide (3.54 μm) and deep (278 nm) wear track of the as-received sample. A much higher steady-state friction coefficient of 14.23±0.58 is detected for the HT-H_2-2h sample as compared with that

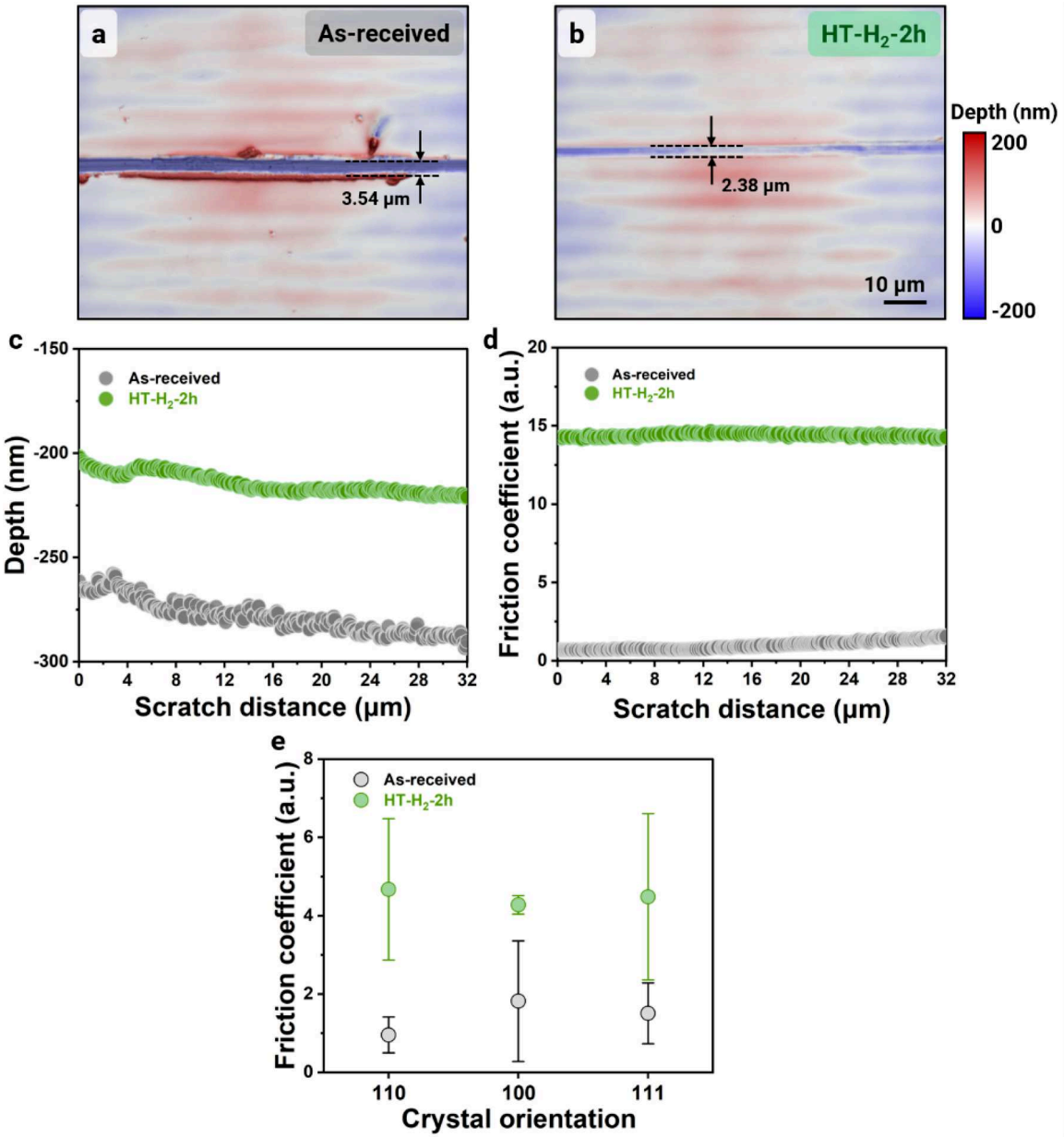

Fig. 7. Three-dimensional profiles of the wear surface of (a) the as-received and (b) HT-H_2-2h samples. (c) The corresponding cross-sectional depth profiles and (d) friction coefficients as a function of the scratch distance. (e) Averaged friction coefficients of the as-received and HT-H_2-2h samples, primarily from the (110), (100), and (111) crystallographic planes.

of the as-received sample (1.66±0.42, Fig. 7d), which is primarily attributed to the spinodal decomposition [58,59]. It is worth noting that such a higher steady-state coefficient for the HT-H_2-2h sample is independent of crystallographic orientation (Fig. 7e). Moreover, yield strength and plastic properties are evaluated based on scratch tests (see Supplementary Note 2) [60,61]. Compared with the estimated yield strength of the as-received sample (929 MPa), an increase in yield strength by 401 MPa is observed in the HT-H_2-2h sample. Additionally, the HT-H_2-2h sample possesses a higher strain hardening exponent of 0.153 than that of the as-received sample of 0.146. Such a higher strain hardening exponent implies a stronger work-hardening effect in the HT-H_2-2h sample. These two examples (*i.e.,* enhancement in hardness and wear resistance) demonstrate that the hydrogen-assisted spinodal decomposition is an effective tool to tailor the mechanical properties of TiNbZrHfTa CCAs.

4. Discussions

The preferential spinodal decomposition in specimens treated in a hydrogen atmosphere poses one intriguing question regarding the role of hydrogen in this phase decomposition process. To unravel the underlying mechanisms of hydrogen-assisted spinodal decomposition, we next assess the role of hydrogen from both the thermodynamic and kinetic perspectives. Thermodynamically, Gibbs free energy was calculated by adopting a sub-regular solution model considering the chemical complexity of the present system (see Supplementary Information Note 3) [42,62]:

$$G = G^{id} + G^{ex} \tag{2}$$

where, G^{id} and G^{ex} represent the ideal Gibbs free energy and excess Gibbs free energy, respectively. Here, G^{id} takes the form of a weighted average of all the alloying elements:

$$G^{id} = \sum_i x_i G_i \tag{3}$$

where, x_i and G_i are referred to as the atomic percentage of i element in the alloy system including hydrogen (which satisfies $\sum_i x_i = 1$) and the corresponding ideal Gibbs free energy respectively. For the sake of simplicity, we assume $x_{Zr} = x_{Ti} = x_{Hf}$, and $x_{Ta} = x_{Nb}$, according to the elemental separation tendency. For hydrogen, its content (x_H) is fixed either 0 at.% (for as-received condition) or a constant of 8.60 at.% (for HT-H_2 condition), consistent with the total hydrogen content measured by TDS in the HT-H_2 sample. The G^{ex} is the excess Gibbs free energy contribution due to the mutual interaction of binary, ternary, quaternary, and quinary elements as well as the senary interactive contribution:

$$G^{ex} = G^{ex}_{binary} + G^{ex}_{ternary} + G^{ex}_{quaternary} + G^{ex}_{quinary} + G^{ex}_{senary} \tag{4}$$

To avoid redundancy in the main text, the analytical details regarding the calculation of Gibbs free energy as well as the corresponding interaction parameters are all summarized in Supplementary

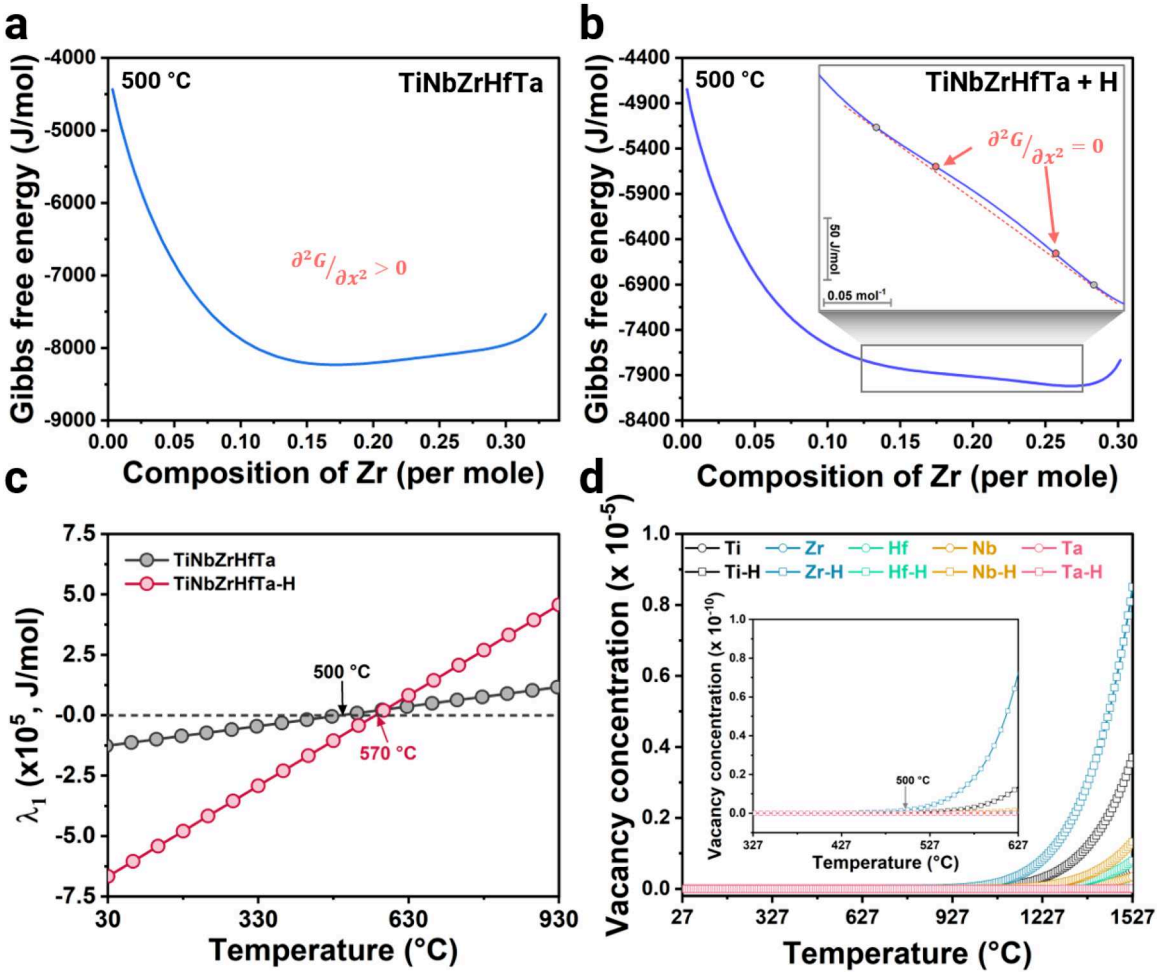

Fig. 8. Zr composition dependence of Gibbs free energy in the TiZrHf-NbTa pseudo-binary system (a) without and (b) with the presence of hydrogen. Insert in (b) showing the existence of miscibility gap, indicated by the points where the second derivative of Gibbs free energy with respect to Zr composition is 0. (c) Eigenvalues (λ_1) as a function of temperature for TiNbZrHfTa with and without the incorporation of hydrogen. (d) Calculated vacancy concentration as a function of temperature.

Note 3. As illustrated in the Gibbs free energy landscape as a function of Zr composition (Figs. 8a and b), the incorporation of hydrogen into the alloy changes the free energy landscape of the TiNbZrHfTa alloy, revealing a characteristic double-well potential with a region of negative curvature in between the local free energy minima, which are delineated by the chemical spinodal points $\partial^2 G/\partial x^2 = 0$. The equiatomic TiNbZrHfTa composition falls in between the spinodal point. Moreover, the eigenvalues (λ_1) of the Hessian matrix were calculated to assess the extent of the thermodynamic effect of hydrogen on spinodal decomposition in this multicomponent alloy system (Fig. 8c) [63]. A positive λ_1 indicates a stable configuration, while the phase instability is reflected by a negative λ_1. The results suggest that spinodal decomposition can occur in the TiNbZrHfTa alloy system without the presence of hydrogen below the critical temperature point (~500 °C), implying that the single BCC phase is unstable. A single solid solution is prone to be stabilized by the entropy effect at high temperatures, while it becomes unstable at low temperatures, decomposing into multiple phases [11,64,65]. The stability of a solid solution with multiple elements, particularly those exceeding three, remains a topic of ongoing debate [64,65]. The stability of the initial TiNbZrHfTa alloy system is not the main topic in this study. We, however, note that the addition of hydrogen expands the spinodal region to a high-temperature region, with a critical temperature of 570 °C. The lower λ_1 value with the incorporation of hydrogen (Fig. 8c) suggests a larger driving force for spinodal decomposition as compared with the TiNbZrHfTa alloy system. Thus, spinodal decomposition is prone to occur at 500 °C in the TiNbZrHfTa alloy system in the presence of hydrogen, supporting the experimental observations. Such a change in the spinodal region can also be triggered by a small amount of other interstitials, for instance, 2 at.% of oxygen can control the formation of the spinodal structure by influencing the spinodal gap of the Ti-V-Hf-Nb system [48].

Hydrogen, in this regard, contributes saliently to the activation of spinodal decomposition from a thermodynamic perspective by expanding the spinodal region. This is probably ascribed to the intensively negative mixing enthalpy between hydrogen and the principal elements (<−40 kJ/mol) [32]. The more negative mixing enthalpy values of Zr-H ($\Delta H^{mix}_{ZrH} = -69$ kJ/mol) and Ti-H ($\Delta H^{mix}_{TiH} = -54$ kJ/mol) pairs as compared with those of Nb-H ($\Delta H^{mix}_{NbH} = -46$ kJ/mol) and Ta-H ($\Delta H^{mix}_{TaH} = -46$ kJ/mol) pairs predominantly drive the separation between Zr/Ti and Nb/Ta [32]. These results suggest that hydrogen can result in a significant thermodynamic modification in the TiNbZrHfTa alloy system.

From the kinetic perspective, the introduction of hydrogen increases the vacancy concentration via the reduction of vacancy formation enthalpy, on the one hand, thus facilitating substitutional diffusion via vacancies [66,67]. On the other hand, the formation of hydrogen-vacancy clusters can significantly impede vacancy migration, leading to opposing effects on diffusion [17,68,69]. Since the stagnation in atomic diffusion (*e.g.*, principle elements) does not contribute positively to spinodal decomposition, here we could first focus on the vacancy concentration to evaluate the kinetic effect caused by hydrogen on spinodal decomposition. Therefore, vacancy concentration (C_v^a) was calculated to evaluate the kinetic influence of hydrogen on the activation of spinodal decomposition:

$$C_v^a = exp\left(-\frac{G_f^v}{kT}\right) \approx exp\left(-\frac{H_f^v}{kT}\right) \quad (5)$$

where, H_f^v, k, and T denote the formation enthalpy for vacancy, Boltzmann constant, and absolute temperature, respectively. The calculation details and corresponding vacancy formation enthalpies of the individual principle elements with and without incorporating hydrogen are summarized in Supplementary Note 4 and **Table S5**. As seen in Fig. 8d, there is little difference in vacancy concentration with and without the presence of hydrogen at 500 °C, demonstrating a negligible kinetic effect caused by hydrogen on spinodal decomposition. Thus, the hydrogen-assisted spinodal decomposition is predominantly rationalized by the thermodynamic effect of hydrogen in the TiNbZrHfTa alloy system, which modifies the local thermodynamic landscape of the system and promotes phase separation.

5. Conclusions

In summary, we show that hydrogen can be introduced as an effective tool to modify the local thermodynamics in an equimolar TiNbZrHfTa complex concentrated alloy at 500 °C, facilitating spinodal decomposition. A periodically modulated chemical pattern forms with a wavelength of ~10 nm and consists of one phase enriched in Ti and Zr and the other enriched in Nb and Ta. The needle-like spinodal features are preferentially aligned along <001> directions, to minimize the elastic strain energy of the system. Such a hydrogen-assisted spinodal decomposition is rationalized by the modification of the local thermodynamic landscape by hydrogen, rendering an expanded spinodal region. Moreover, we exemplarily demonstrate that this hydrogen-assisted spinodal decomposition improves the hardness and wear resistance in the alloy system. Thus, we show here a novel strategy to trigger spinodal decomposition by introducing hydrogen as an acquired alloying element from the heat treatment environment, opening up alternative avenues for designing metastable alloys and improving mechanical properties.

Appendix. Supplementary Materials

The supplementary materials associated with this study is available online.

CRediT authorship contribution statement

Chengguang Wu: Writing – review & editing, Writing – original draft, Visualization, Methodology, Investigation, Formal analysis, Data curation, Conceptualization. **Leonardo Shoji Aota:** Writing – review & editing, Formal analysis. **Jing Rao:** Writing – review & editing, Investigation. **Xukai Zhang:** Writing – review & editing, Investigation. **Loïc Perrière:** Writing – review & editing, Investigation. **Maria Jazmin Duarte:** Writing – review & editing, Investigation. **Dierk Raabe:** Writing – review & editing, Supervision, Project administration, Funding acquisition. **Yan Ma:** Writing – review & editing, Supervision, Resources, Project administration, Conceptualization.

Declaration of competing interest

The authors declare that they have no known competing financial interests or personal relationships that could have appeared to influence the work reported in this paper.

Acknowledgments

The kind support from Prof. Jean-Philippe Couzinié and Dr. Shaolou Wei for the fruitful discussions and technical exchanges is greatly acknowledged. We acknowledge DESY (Hamburg, Germany), a member of the Helmholtz Association HGF, for the provision of experimental facilities. Parts of this research were carried out at P02.1, and we would like to thank Dr. Alexander Schökel for his assistance (Proposals I-20230183 and I-20231121). C.G.W. would like to appreciate the kind help on sample preparations and SEM-related characterizations from Katja Angenendt and Christian Broβ at the Max Planck Institute for Sustainable Materials. The kind help on heat treatment from Michael Adamek at the Max Planck Institute for Sustainable Materials is also greatly thankful. C.G.W. gratefully acknowledges the financial support from the China Scholarship Council (Number: 202106780003). Y.M. and D.R. would like to acknowledge the financial funding of Deutsche Forschungsgemeinschaft (DFG) within the Priority Programme SPP2006 (Project number: 388544551).

Supplementary materials

Supplementary material associated with this article can be found, in the online version, at doi:10.1016/j.actamat.2024.120707.

References

[1] D. Raabe, The materials science behind sustainable metals and alloys, Chem. Rev. 123 (5) (2023) 2436–2608.
[2] S.E. Hosseini, M.A. Wahid, Hydrogen production from renewable and sustainable energy resources: promising green energy carrier for clean development, Renew. Sustain. Energy Rev. 57 (2016) 850–866.
[3] A. Kovač, M. Paranos, D. Marciuš, Hydrogen in energy transition: a review, Int. J. Hydrog. Energy 46 (16) (2021) 10016–10035.
[4] S.E. Prameela, T.M. Pollock, D. Raabe, M.A. Meyers, A. Aitkaliyeva, K.-L. Chintersingh, Z.C. Cordero, L. Graham-Brady, Materials for extreme environments, Nat. Rev. Mater. 8 (2) (2023) 81–88.
[5] J.O. Abe, A.P.I. Popoola, E. Ajenifuja, O.M. Popoola, Hydrogen energy, economy and storage: review and recommendation, Int. J. Hydrog. Energy 44 (29) (2019) 15072–15086.
[6] J.C. Zhao, J.H. Westbrook, Ultrahigh-temperature materials for jet engines, MRS Bull. 28 (9) (2003) 622–630.
[7] F. Marques, M. Balcerzak, F. Winkelmann, G. Zepon, M. Felderhoff, Review and outlook on high-entropy alloys for hydrogen storage, Energy Environ. Sci. 14 (10) (2021) 5191–5227.
[8] X. Wang, W. Guo, Y. Fu, High-entropy alloys: emerging materials for advanced functional applications, J. Mater. Chem. A 9 (2) (2021) 663–701.
[9] C. Zlotea, M. Sow, G. Ek, J.-P. Couzinié, L. Perrière, I. Guillot, J. Bourgon, K. Møller, T. Jensen, E. Akiba, Hydrogen sorption in TiZrNbHfTa high entropy alloy, J. Alloy. Compd. 775 (2019) 667–674.
[10] O.N. Senkov, S. Gorsse, D.B. Miracle, High temperature strength of refractory complex concentrated alloys, Acta Mater. 175 (2019) 394–405.
[11] F. Sun, G. Miyamoto, Y. Liu, Y. Hayasaka, T. Furuhara, Phase separation with ordering in aged Fe-Ni-Mn medium entropy alloy, Acta Mater. 223 (2022) 117487.
[12] E.P. George, D. Raabe, R.O. Ritchie, High-entropy alloys, Nat. Rev. Mater. 4 (8) (2019) 515–534.
[13] E.P. George, W.A. Curtin, C.C. Tasan, High entropy alloys: a focused review of mechanical properties and deformation mechanisms, Acta Mater. 188 (2020) 435–474.
[14] P.T. Hung, M. Kawasaki, J.-K. Han, J.L. Lábár, J. Gubicza, Thermal stability of a nanocrystalline HfNbTiZr multi-principal element alloy processed by high-pressure torsion, Mater. Charact. 168 (2020) 110550.
[15] Y. Guo, J. He, W. Lu, L. Jia, Z. Li, The evolution of compositional and microstructural heterogeneities in a TaMo0.5ZrTi1.5Al0.1Si0.2 high entropy alloy, Mater. Charact. 172 (2021) 110836.
[16] Y. Cao, W. Zhang, B. Liu, Y. Liu, M. Du, A. Fu, Phase decomposition behavior and its effects on mechanical properties of TiNbTa0.5ZrAl0.5 refractory high entropy alloy, J. Mater. Sci. Technol. 66 (2021) 10–20.
[17] Y. Fukai, The Metal-Hydrogen System: Basic Bulk Properties, Springer Science & Business Media, 2006.
[18] H.-J. Christ, M. Decker, S. Zeitler, Hydrogen diffusion coefficients in the titanium alloys IMI 834, Ti 10-2-3, Ti 21 S, and alloy C, Metal. Mater. Trans. A 31 (2000) 1507–1517.
[19] K. Hirata, S. Iikubo, M. Koyama, K. Tsuzaki, H. Ohtani, First-principles study on hydrogen diffusivity in BCC, FCC, and HCP iron, Metal. Mater. Trans. A 49 (10) (2018) 5015–5022.
[20] J. Völkl, G. Alefeld, Diffusion of hydrogen in metals, Hydrogen in Metals I: Basic Properties (2005) 321–348.
[21] S. Trasatti, Electronegativity, work function, and heat of adsorption of hydrogen on metals, J. Chem. Soc. Faraday Trans. 1 68 (1972) 229–236. : Physical Chemistry in Condensed Phases.
[22] S.K. Dwivedi, M. Vishwakarma, Hydrogen embrittlement in different materials: a review, Int. J. Hydrog. Energy 43 (46) (2018) 21603–21616.
[23] I.M. Robertson, P. Sofronis, A. Nagao, M.L. Martin, S. Wang, D. Gross, K. Nygren, Hydrogen embrittlement understood, Metal. Mater. Trans. A 46 (2015) 2323–2341.
[24] P. Cotterill, The hydrogen embrittlement of metals, Prog. Mater. Sci. 9 (4) (1961) 205–301.
[25] L. Luo, L. Chen, L. Li, S. Liu, Y. Li, C. Li, L. Li, J. Cui, Y. Li, High-entropy alloys for solid hydrogen storage: a review, Int. J. Hydrog. Energy 50 (2024) 406–430.
[26] T.R. Somo, M.V. Lototskyy, V.A. Yartys, M.W. Davids, S.N. Nyamsi, Hydrogen storage behaviours of high entropy alloys: a review, J. Energy Storage 73 (2023) 108969.
[27] B.H. Toby, R.B. Von Dreele, GSAS-II: the genesis of a modern open-source all purpose crystallography software package, J. Appl. Crystallogr. 46 (2) (2013) 544–549.
[28] M. Hÿtch, E. Snoeck, R. Kilaas, Quantitative measurement of displacement and strain fields from HREM micrographs, Ultramicroscopy 74 (3) (1998) 131–146.
[29] E. Zuzek, J. Abriata, A. San-Martin, F. Manchester, The H-Zr (hydrogen-zirconium) system, Bull. Alloy Phase Diagrams 11 (4) (1990) 385–395.
[30] D.R. McKenzie, Y. Yin, W.D. McFall, N.H. Hoang, The orientation dependence of elastic strain energy in cubic crystals and its application to the preferred orientation in titanium nitride thin films, J. Phys. Condens. Matter 8 (32) (1996) 5883.
[31] D. Seol, S. Hu, Y. Li, J. Shen, K. Oh, L. Chen, Computer simulation of spinodal decomposition in constrained films, Acta Mater. 51 (17) (2003) 5173–5185.
[32] A. Takeuchi, A. Inoue, Classification of bulk metallic glasses by atomic size difference, heat of mixing and period of constituent elements and its application to characterization of the main alloying element, Mater. Trans. 46 (12) (2005) 2817–2829.
[33] A. Shariq, T. Al-Kassab, R. Kirchheim, Studying nearest neighbor correlations by atom probe tomography (APT) in metallic glasses as exemplified for Fe40Ni40B20 glassy ribbons, J. Alloy. Compd. 512 (1) (2012) 270–277.
[34] T. Philippe, F. De Geuser, S. Duguay, W. Lefebvre, O. Cojocaru-Mirédin, G. Da Costa, D. Blavette, Clustering and nearest neighbour distances in atom-probe tomography, Ultramicroscopy 109 (10) (2009) 1304–1309.
[35] D.E. Perea, I. Arslan, J. Liu, Z. Ristanović, L. Kovarik, B.W. Arey, J.A. Lercher, S. R. Bare, B.M. Weckhuysen, Determining the location and nearest neighbours of aluminium in zeolites with atom probe tomography, Nat. Commun. 6 (1) (2015) 7589.
[36] M.P. Moody, L.T. Stephenson, A.V. Ceguerra, S.P. Ringer, Quantitative binomial distribution analyses of nanoscale like-solute atom clustering and segregation in atom probe tomography data, Microsc. Res. Tech. 71 (7) (2008) 542–550.
[37] R. Hu, S. Jin, G. Sha, Application of atom probe tomography in understanding high entropy alloys: 3D local chemical compositions in atomic scale analysis, Prog. Mater. Sci. 123 (2022) 100854.
[38] R.W. Balluffi, S.M. Allen, W.C. Carter, Kinetics of Materials, John Wiley & Sons, 2005.
[39] G. Gottstein, Physical Foundations of Materials Science, Springer, 2004.
[40] T. Philippe, P.W. Voorhees, Ostwald ripening in multicomponent alloys, Acta Mater. 61 (11) (2013) 4237–4244.
[41] T. Philippe, D. Blavette, P. Voorhees, Critical nucleus composition in a multicomponent system, J. Chem. Phys. 141 (12) (2014).
[42] C.H. Lupis, Chemical Thermodynamics of Materials, Elsevier Science Publishing Co., Inc, 1983.
[43] Z. Rao, B. Dutta, F. Körmann, W. Lu, X. Zhou, C. Liu, A.K. da Silva, U. Wiedwald, M. Spasova, M. Farle, Beyond solid solution high-entropy alloys: tailoring magnetic properties via spinodal decomposition, Adv. Funct. Mater. 31 (7) (2021) 2007668.
[44] M. Hetherington, M. Miller, On the statistical analysis of atom probe data, J. Phys. Colloq. 48 (C6) (1987). C6-559-C6-564.
[45] D. Blavette, F. Vurpillot, P. Pareige, A. Menand, A model accounting for spatial overlaps in 3D atom-probe microscopy, Ultramicroscopy 89 (1–3) (2001) 145–153.
[46] W.M. Haynes, CRC Handbook of Chemistry and Physics, CRC Press, 2016.
[47] T. Xin, Y. Zhao, R. Mahjoub, J. Jiang, A. Yadav, K. Nomoto, R. Niu, S. Tang, F. Ji, Z. Quadir, Ultrahigh specific strength in a magnesium alloy strengthened by spinodal decomposition, Sci. Adv. 7 (23) (2021) eabf3039.
[48] D. Cui, Y. Zhang, L. Liu, Y. Li, L. Wang, Z. Wang, J. Li, J. Wang, F. He, Oxygen-assisted spinodal structure achieves 1.5 GPa yield strength in a ductile refractory high-entropy alloy, J. Mater. Sci. Technol. 157 (2023) 11–20.
[49] B.G. Yuan, C.F. Li, H.P. Yu, D.L. Sun, Influence of hydrogen content on tensile and compressive properties of Ti–6Al–4V alloy at room temperature, Mater. Sci. Eng. A 527 (16) (2010) 4185–4190.
[50] W.R. Kerr, The effect of hydrogen as a temporary alloying element on the microstructure and tensile properties of Ti-6Al-4V, Metal. Trans. A 16 (1985) 1077–1087.
[51] H.J. Christ, A. Senemmar, M. Decker, K. Prü\ner, Effect of hydrogen on mechanical properties of β -titanium alloys, Sadhana 28 (3) (2003) 453–465.
[52] W. Soboyejo, Mechanical Properties of Engineered Materials, CRC Press, 2002.
[53] J. Waisman, G. Sines, L. Robinson, Diffusion of hydrogen in titanium alloys due to composition, temperature, and stress gradients, Metal. Trans. 4 (1973) 291–302.
[54] M. Kato, Hardening by spinodally modulated structure in bcc alloys, Acta Metal. 29 (1) (1981) 79–87.
[55] W. Petry, A. Heiming, J. Trampenau, M. Alba, C. Herzig, H. Schober, G. Vogl, Phonon dispersion of the bcc phase of group-IV metals. I. bcc titanium, Phys. Rev. B 43 (13) (1991) 10933.
[56] D. Tabor, The physical meaning of indentation and scratch hardness, Br. J. Appl. Phys. 7 (5) (1956) 159.
[57] Y. Luo, Q. Pan, Y. Sun, S. Liu, Y. Sun, L. Long, X. Li, X. Wang, M. Li, Hardening behavior of Al-0.25Sc and Al-0.25Sc-0.12Zr alloys during isothermal annealing, J. Alloys Compd. 818 (2020) 152922.
[58] R. Rachbauer, S. Massl, E. Stergar, D. Holec, D. Kiener, J. Keckes, J. Patscheider, M. Stiefel, H. Leitner, P.H. Mayrhofer, Decomposition pathways in age hardening of Ti-Al-N films, J. Appl. Phys. 110 (2) (2011).
[59] Z. An, S. Mao, T. Yang, C.T. Liu, B. Zhang, E. Ma, H. Zhou, Z. Zhang, L. Wang, X. Han, Spinodal-modulated solid solution delivers a strong and ductile refractory high-entropy alloy, Mater. Horiz. 8 (3) (2021) 948–955.
[60] S. Bellemare, M. Dao, S. Suresh, A new method for evaluating the plastic properties of materials through instrumented frictional sliding tests, Acta Mater. 58 (19) (2010) 6385–6392.
[61] A. Prasad, M. Dao, S. Suresh, Steady-state frictional sliding contact on surfaces of plastically graded materials, Acta Mater. 57 (2) (2009) 511–524.
[62] S. Wei, C.C. Tasan, Deformation faulting in a metastable CoCrNiW complex concentrated alloy: a case of negative intrinsic stacking fault energy? Acta Mater. 200 (2020) 992–1007.
[63] K. Kadirvel, S.R. Koneru, Y. Wang, Exploration of spinodal decomposition in multi-principal element alloys (MPEAs) using CALPHAD modeling, Scr. Mater. 214 (2022) 114657.
[64] S. Wei, F. He, C.C. Tasan, Metastability in high-entropy alloys: a review, J. Mater. Res. 33 (19) (2018) 2924–2937.

[65] S.A. Kube, J. Schroers, Metastability in high entropy alloys, Scr. Mater. 186 (2020) 392–400.
[66] E. Veleckis, R.K. Edwards, Thermodynamic properties in the systems vanadium-hydrogen, niobium-hydrogen, and tantalum-hydrogen, J. Phys. Chem. 73 (3) (1969) 683–692.
[67] K. Wang, X. Kong, J. Du, C. Li, Z. Li, Z. Wu, Thermodynamic description of the Ti–H system, CALPHAD 34 (3) (2010) 317–323.
[68] H.-X. Huang, Y.-H. Li, Z.-Z. Li, P.-W. Hou, F.-F. Ma, Q.-Y. Ren, H.-B. Zhou, G.-H. Lu, Role of hydrogen in stability and mobility of vacancy clusters in tungsten, Tungsten 4 (3) (2022) 219–230.
[69] L. Ismer, M.S. Park, A. Janotti, C.G. Van de Walle, Interactions between hydrogen impurities and vacancies in Mg and Al: a comparative analysis based on density functional theory, Phys. Rev. B 80 (18) (2009) 184110.